Energy Conversion and Management 340 (2025) 119974

Contents lists available at ScienceDirect

Energy Conversion and Management

journal homepage: www.elsevier.com/locate/enconman

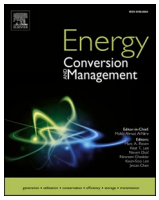

Research Paper

A novel solids-based electro-thermal energy storage system utilizing electromagnetic induction: Conceptual design and theoretical analysis

Weiqin Lu [a], Xueyu Tang [a], Yang Zhang [a,b,c], Weiliang Wang [d], Tuo Zhou [a], Hai Zhang [a], Junfu Lyu [a,b,c], Xiwei Ke [b,c,*]

[a] Key Laboratory for Thermal Science and Power Engineering of Ministry of Education, Department of Energy and Power Engineering, Tsinghua University, Haidian District, 100084 Beijing, China
[b] Beijing Huairou Laboratory, Beijing 101499, China
[c] Shanxi Research Institute of Huairou Laboratory, Taiyuan 101499, China
[d] Key Lab of Disaster and Control in Engineering, International Energy School (Energy and Electricity Research Center), Jinan University, Zhuhai 519070, China

ARTICLE INFO

Keywords:
Electromagnetic induction heat storage
Moving bed heat release
Thermal and economic analyses
System design
Numerical simulation

ABSTRACT

Electro-thermal energy storage (ETES) technology has presented its great potential to efficiently consume renewable energy and increase the flexibility of power grid. This paper presents an innovative ETES system that integrates electromagnetic induction heat storage (EIHS) with moving bed heat release (MBHR). A numerical simulation method based on CFD-DEM was developed to access the system's performance and evaluate its technical feasibility. In a studied case, the EI heater unit achieves uniform radial temperature distribution, adjustable temperature rise rate, and high particle heat storage density, while the tubular MBHE unit shows high heat transfer intensity (678.2–784.6 $W/m^2/K$). The system's power-to-power conversion efficiency is approximately 30.78 %, excluding minor power consumption. The developed system offers three operation modes and two business models for peak electricity supply. The preliminary economic evaluation indicates that model 1, using valley power, has a 5-year payback period and a 21.56 % internal rate of return (*IRR*), while model 2, using abandoned photovoltaic/wind power, shows a 10-year payback period and an 11.26 % *IRR*. Further sensitivity analysis suggests model 1 is more cost-effective while model 2 offers slightly better risk resistance. This work has offered some valuable insights into the advanced enhancement and development of the ETES system, as well as its future engineering applications.

1. Introduction

Currently, renewable energy sources such as photovoltaic and wind power have experienced rapid development. Global renewable capacity additions are projected to increase from 666 GW in 2024 to about 935 GW in 2030, with photovoltaic and wind power forecast to make up 95 % of the total renewable capacity growth during this period [1]. However, these high-proportion renewable energy sources, characterized by intermittency, volatility, and randomness, significantly impact the reliability and stable operation of the power grid [2–4]. Consequently, a variety of energy storage technologies have emerged, with the core objective of storing surplus power in alternative energy forms (such as thermal energy [5], chemical energy [6,7], mechanical energy [8,9], etc.) and subsequently deploying it as heat or electricity in response to demand when necessary. Among various forms of energy storage methods, electro-thermal energy storage (ETES) technology has garnered significant attention due to its system simplicity, high efficiency in electro-thermal conversion, and broad applicability. For instance, in terms of a photovoltaic power station coupled with hydrogen production from water electrolysis, the addition of an ETES system can effectively mitigate the intermittency of photovoltaic power and enhance the supply stability of the hydrogen production [10,11]. For the coal-fired generation units, the ETES system can efficiently consume the electricity in excess of load demand, thereby significantly enhancing their peak shaving capacity [12]. Furthermore, it can function as an independent energy storage power station (electric-to-thermal-to-electric conversion) [13,14], or satisfy the heat needs of users (such as paper mills) [15], in order to mitigate the imbalance and instability of electricity supply and demand, thus substantially boosting the grid's flexibility.

Generally, an ETES system can be characterized by three key parts,

* Corresponding author at: Beijing Huairou Laboratory, Beijing 101499, China.
E-mail address: kexiwei@sxri.hrl.ac.cn (X. Ke).

https://doi.org/10.1016/j.enconman.2025.119974
Received 4 March 2025; Received in revised form 10 May 2025; Accepted 18 May 2025
Available online 28 May 2025

Nomenclature

Area	heat transfer area, m^2
B_0	Amplitude of the incident magnetic flux density, mT
B_m	Coefficient related to the business models, /
C	Annual total cost, $\times 10^4$ ¥/y
C_{pf}	Fluid specific heat capacity, J/kg/K
C_{pp}	Particle specific heat capacity, J/kg/K
D_c	Coil inner diameter, m
d_p	Particle diameter, m
e	Earnings, ¥/kW·h
Fij	Critical parameters in the evaluation model, /
f	Heating frequency, Hz
h	Hours, h
h_c	Coil height, m
h_{coef}	Heat transfer coefficient, $W/m^2/K$
I	Investment, $\times 10^4$ ¥
I_c	Coil maximum current, A
K	Correction coefficient, /
L_c	Project life cycle, y
M_x	Money flow over x years, /
$\dot{m}$	Rated mass flow rate, t/h or kg/s
m	Mass, kg
N_H	Number of EI heater units, /
N_p	Number of particles in an EI heater unit, /
n_w	Number of workers, /
n_{min}	A parameter related to the payback period *PBP*, y
P	Power, kW
p	Price, ¥/t or $\times 10^4$ ¥/t
Q_{f-w}	Fluid-to-wall heat flux, W
Q_{px}	Particle heat flux involving conduction, convection, and radiation
Q_{p-w}	Particle-to-wall heat flux, W
Q_w	Heat flux received by tube wall, W
r	Ratio or interest rate, /
S_{ij}	Sensitivity coefficient of factor *Fij*, /
$\overline{S_{ij}}$	Average sensitivity coefficient of multiple tests, /
T_c	Turns per coil, /
T_f	Fluid temperature, K
T_p	Particle temperature, K
ΔT_{p-w}	Particle-to-wall temperature difference, K
t	Time, s
V	Particle volume, m^3
v_{des}	Particle descending velocity in an EI heater unit, mm/s
W_H	Internal heat source strength, W
w_s	average salary of a single worker per year, $\times 10^4$ ¥/y
Y	Annual total revenue, $\times 10^4$ ¥/y (Wan Yuan per year)
Y_{net}	Annual net profit, $\times 10^4$ ¥

Greek letters

α_f	Packed bed porosity, /
ρ_f	Fluid density, kg/m^3
ρ_p	Particle density, kg/m^3
δ_s	Skin thickness, m
η	Efficiency or coefficient, /
$\Delta\varphi$	Enthalpy change, kJ/kg

Subscripts

ao	Actual output of steam turbine
ap	Actual power
cs	Comprehensive subsidy
EIh	EI heating
e	Equipment
ei	Equipment installation
em	Equipment maintenance
et	Engineering test
go	Generator output
gs	Government subsidy
hr	Heat release
hs	Heat storage
hu	Heat utilization in the tubular MBHE
hw	Hiring workers
l	Land
op	Operating
p	Particle
pd	Project design
pe	Peak electricity
pg	Power generation
pm	Project management
pp	Peak power demand for self-consumption
rp	Rated power of steam turbine
s	Steam
scp	Self-consumption power
sp	Supplement particle
sw	Supplement water
t	Total
v	Valley electricity
ve	Valley electricity
w	Water

Abbreviations

AC	Alternating current
CFD-DEM	Combined approach of computational fluid dynamics and discrete element method
EI	Electromagnetic induction
EIHS-MBHR	EI heat storage with moving bed heat release
ETES	Electro-thermal energy storage
FBHE	Fluidized bed heat exchanger
H2H	Heat-to-heat
H2H2P	Heat-to-heat-to-power
H2X	Heat-to-x, X/x can be electricity, thermal energy, or even chemical energy
IRR	Internal rate of return
MBHE	Moving bed heat exchanger
NPV	Net present value
P2H	Power-to-heat
P2P	Power-to-power
PBP	Payback period
PICM	Particle-in-cell method
TFM	Two-fluid method
SM	Supplementary Material

which are the power-to-heat (P2H) module, the medium used in the heat storage & release cycle (such as molten salt, silica sand, water, etc.), and the heat-to-x (H2X) energy conversion/transfer module (X can be electricity, thermal energy, or even chemical energy). For instance, within the built environment sector, heat pumps or electric boilers are frequently utilized as power-to-heat (P2H) technologies to transform electricity into thermal energy, while the medium for this conversion can be either water or air with an indoor heat exchanger serving as a H2X device [16]. When it comes to P2H technology, the main heating methods include resistance heating based on direct-current Joule effect

[14], electrical infrared heating using thermal radiation, high-frequency heating employing microwaves, and inductive heating utilizing electromagnetic induction (EI) effect [16]. Among these, the resistance heating method has garnered enough attention due to its advantages of system simplicity, convenient operation, and wide applicability [3,17]. However, further engineering applications of the resistance heating method are constrained by its inherent drawbacks, including uneven heating (only directly heat materials around heating surface), finite lifespan of resistance materials (harsh operating conditions), and the potential for introducing impurities into the circulating medium (overheating of resistance materials) [16]. In contrast to the resistance heating method, the inductive heating method excels due to its intrinsic advantages including cost-effectiveness, rapid heating response, precise temperature control, operation safety, and the absence of pollution [18–20]. Hence, this method has been extensively applied to the metal heat treatment, the metal melting, and the metal welding. Accordingly, it holds significant potential within the energy storage domain, yet it currently gains limited attention, with the feasible implementation strategies and system configurations still being undefined.

While, it is essential to confirm the uniformity of EI heating within a densely packed bed. As reported, within the research domain of pebble bed systems with internal heat generation [21–26], enough experiments have demonstrated that an EI coil with a certain number of turns can effectively and uniformly heat the steel pellets inside it. Catton and Jakobsson [24] observed that under the conditions of a 463 kHz heating frequency, a 61 mm i.d. glass tube, and steel particles with the diameters of 0.69 mm, 1.6 mm, 3.2 mm, and 4.8 mm, the spatial power distribution within their EI heater was nearly uniform in both the axial and radial directions. Afterwards, the experiments carried out by Patrick et al. [25,26] and Sun et al. [23,27] also demonstrated this uniformly heating effect within EI heaters, despite their different operating conditions. Thus, it has been confirmed that employing an EI heater as P2H equipment, along with conductive particles as the medium for heat storage and release, and utilizing a tubular MBHE for particle heat release, is a viable approach.

In the EI heating process, high-frequency alternating current (AC) is applied to the coils, generating an alternating magnetic field. Within this field, the EI effect induces numerous eddy currents in conductive materials, leading to continuous heating through the Joule effect. However, common heat storage/release media (include solid particles like desert sand [28], rocks, gravel [29], and liquids like molten salts, conduction oil [30]) cannot be directly heated through the EI effect since they are nonconducting. Given this, an ideal circulating medium should process the following properties: satisfactory electrical conductivity, high thermal conductivity, suitable specific heat capacity, high melting point, low Curie point or weak magnetism, and acceptable cost. Nevertheless, the EI heating process is particularly characterized by a unique magnetic shielding phenomenon. Liu et al. [2] utilized a metallic heat exchanger tube enveloped by an external electromagnetic coil to facilitate inductive heating. Due to the magnetic shielding phenomenon, upon activation, the coil only induces a gradual temperature rise in the metallic tube wall, rather than in the iron ore particles. Thus, it is necessary to carefully design the system and select the appropriate materials to fully exploit the excellent characteristics of EI heating.

In order to facilitate the heat release or H2X conversion/transfer process, two main configurations of heat exchangers are used at present: fluidized bed and moving bed. The fluidized bed heat exchanger (FBHE) features its strong gas–solid heat transfer capacity, high heat release rate, and cost-effectiveness due to the needless of heat transfer surfaces [31,32]. Moreover, recent research conducted by the National Renewable Energy Laboratory suggests that integrating the FBHE with a high-efficiency air-Brayton combined cycle power block holds significant promise [32–34]. However, it is not applicable for the ETES system utilizing EI heating method, due to the fact that the large and dense conductive particles are difficult to be fluidized while the fine powders may lead to poor heating performance due to the magnetic shielding effect. Additionally, it is crucial to address challenges such as particle wear, increased self-electricity consumption, and gas heat loss, as these are also significant concerns that warrant attention [31]. Compared to the FBHE, the moving bed heat exchanger (MBHE), especially tubular MBHE, appears better applicability, owing to their compact design, acceptable heat loss, economic feasibility, and adeptness at managing solid particles [35–37]. Therefore, tubular MBHEs are extensively employed for waste heat recovery from high-temperature solids generated by industrial processes, such as sinters in steel-making [38].

When evaluating a new ETES system, numerical simulation methods, in addition to essential experiments, can offer a more detailed analysis of the multi-physical fields within the system and access its comprehensive performance. Furthermore, numerical simulation methods can also provide theoretical guidance for the optimization of system structure and operational parameters. Nowadays, the mainstream multiphase flow models include the two-fluid method (TFM), the particle-in-cell method (PICM), and the combined approach of computational fluid dynamics and discrete element method (CFD-DEM). Among these methods, CFD-DEM, which treats the fluid phase as continuous and the particle phase as discrete, offers the benefits of interpretability and authenticity, making it particularly suited to simulate the heat and mass transfer phenomena in ETES systems. Furthermore, scholars have developed various extensions to the CFD-DEM to study the gas–solid system operating in different application scenarios. However, there is a lack of heat transfer model integrated into the CFD-DEM framework to accurately resolve the EI heating phenomenon without any electromagnetic simulation.

Given these, an innovative ETES technology combining EI heat storage with moving bed heat release, named as EIHS-MBHR, is firstly proposed in this paper. The system description and possible engineering applications are described in detail. In addition, a numerical simulation method based on CFD-DEM is established with preliminary verification to study the particle heating process in an EI heater and the heat release process in a tubular MBHE. Finally, a comprehensive economic evaluation, incorporating a detailed sensitivity analysis, of this conceptual ETES is conducted to further assess its feasibility.

2. EIHS-MBHR system design and application

2.1. System description

2.1.1. System design

The conceptual EIHS-MBHR system is shown in Fig. 1, which is detailed as follows. As mentioned above, a standard EIHS-MBHR system primarily comprises three modules: a P2H module, a heat-to-heat (H2H) or heat-to-heat-to-power (H2H2P) module, and a particle storage and transport module.

(1) The P2H module consists of an EI heater, an AC power, a frequency converter, and a temperature controller with several thermocouples. The EI heater is powered by the equipped AC supply, whose frequency is controlled by the converter. A temperature controller monitors and adjusts the heater's internal temperature to prevent overheating;
(2) The H2H module for heat provision includes a tubular MBHE and a water pump. The water is heated to the desired temperature and then distributed to heat users via the pipeline system. While, the H2H2P module, which addresses power demand, covers a tubular MBHE, a water pump, a steam turbine, an electric generator, and a steam condenser. A conventional steam Rankine cycle is utilized, and the generated electricity is subsequently allocated to electricity users;
(3) The particle storage and transport module encompasses an elevator for particles, several solid flow controllers for discharge, a hot bulk storage unit, and a cold bulk storage unit. The solid flow controllers are designed to precisely regulate the flow rate at

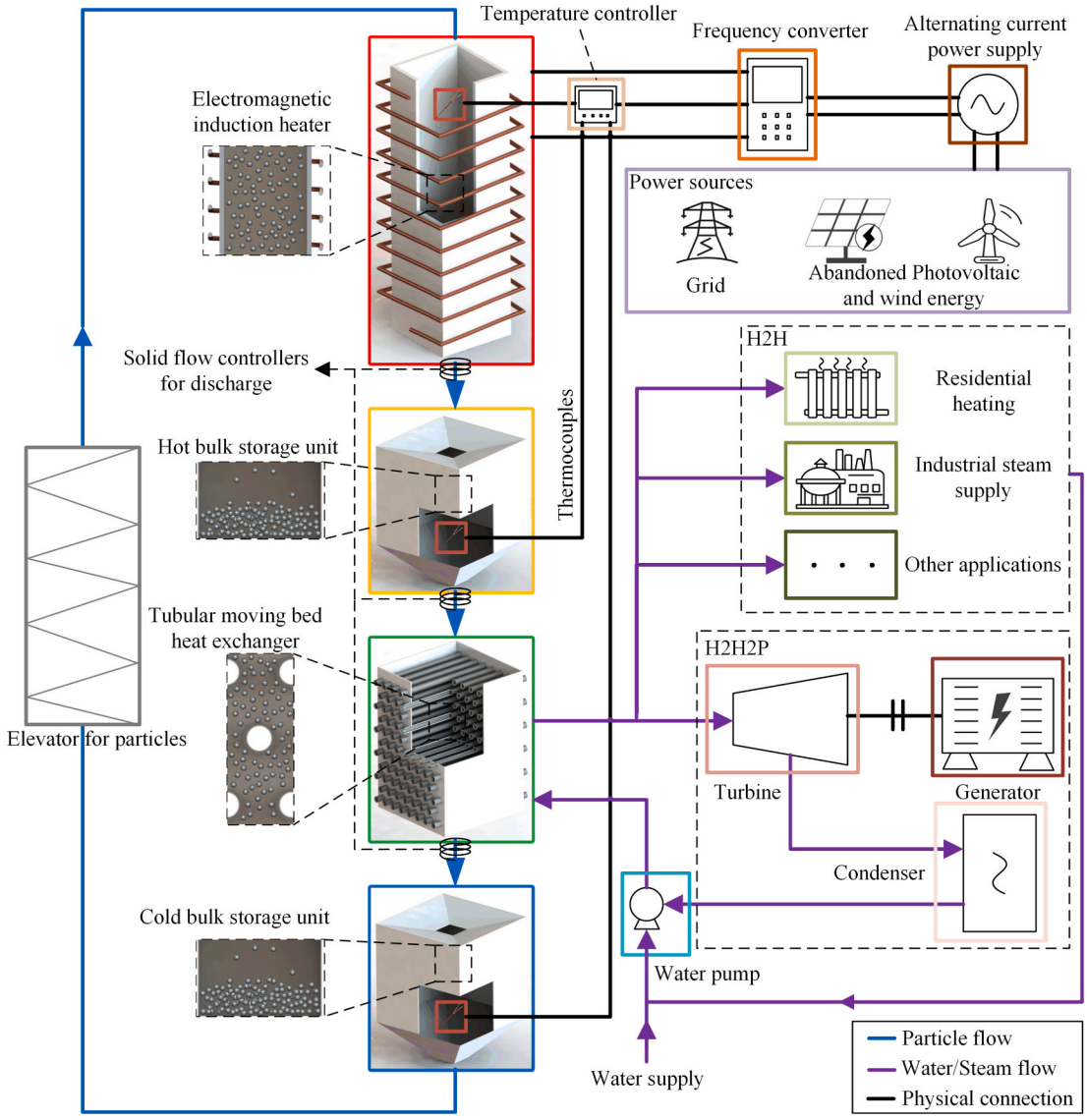

Fig. 1. A schematic of the EIHS-MBHR system.

the outlets of these devices. The hot bulk storage unit acts as an insulator, effectively maintaining the temperature of the internal particles.

(4) Additionally, the system includes various supplementary parts, such as a coil radiator and connecting fittings.

For the particle cycle, the bed materials, such as millimeter-grade steel pellets, are lifted by the carrier and then fed into the heater through its top inlet. Meanwhile, the input power's frequency is converted from the industrial frequency to a specific high frequency through a frequency converter, and then the electricity is transferred into the multiturn coil wrapped around the heater. As a result of the EI effect, the particles are heated by eddy currents, and their temperature can be efficiently maintained at a high level (>600 ℃).

After the heating process, the high temperature particles are transferred to the hot bulk storage unit. If required, the hot particles can be directed into the tubular MBHE for heat release, immediately transferring their sensible heat to the working medium (water or steam) flowing in tube banks. In the tubular MBHE, the particles are driven by their gravity and move slowly at a set low descent velocity. Afterwards, the colder particles descend into the cold bulk storage unit to await being lifted back into the heater, thus completing the material cycle.

As for the fluid medium, a typical steam Rankine cycle is employed. Detailly, the supercooled water is introduced into the tubular MBHE and absorbs sensible heat from the high-temperature steel pellets. Then, the produced superheated steam can be applied by the heat users directly, or it can drive the steam turbine for electricity generation. For the latter situation, the dead steam condenses into the supercooled water in the condenser, and then participates in the next fluid medium cycle.

2.1.2. *Operational modes*

As illustrated in Fig. 2, for this EIHS-MBHR system, there are mainly three potential operation modes towards different application scenarios, which are batch operation mode (Fig. 2a), semi-continuous operation mode (Fig. 2b), and continuous operation mode (Fig. 2c).

(1) In the batch operation mode, the operating processes can be divided into four stages: particle lifting stage, particle heating stage, heat storage stage, and heat release stage. In the first stage, the particle elevator is running and lifting the particles from the cold bulk storage unit into the EI heater for particle packing. When the excess electricity is available, the second stage starts, resulting in the particles inside the heater heated to a high temperature level. Since the average particle temperature reaches the set value, the third stage operates and the heated particles are transferred to the hot bulk storage unit for heat

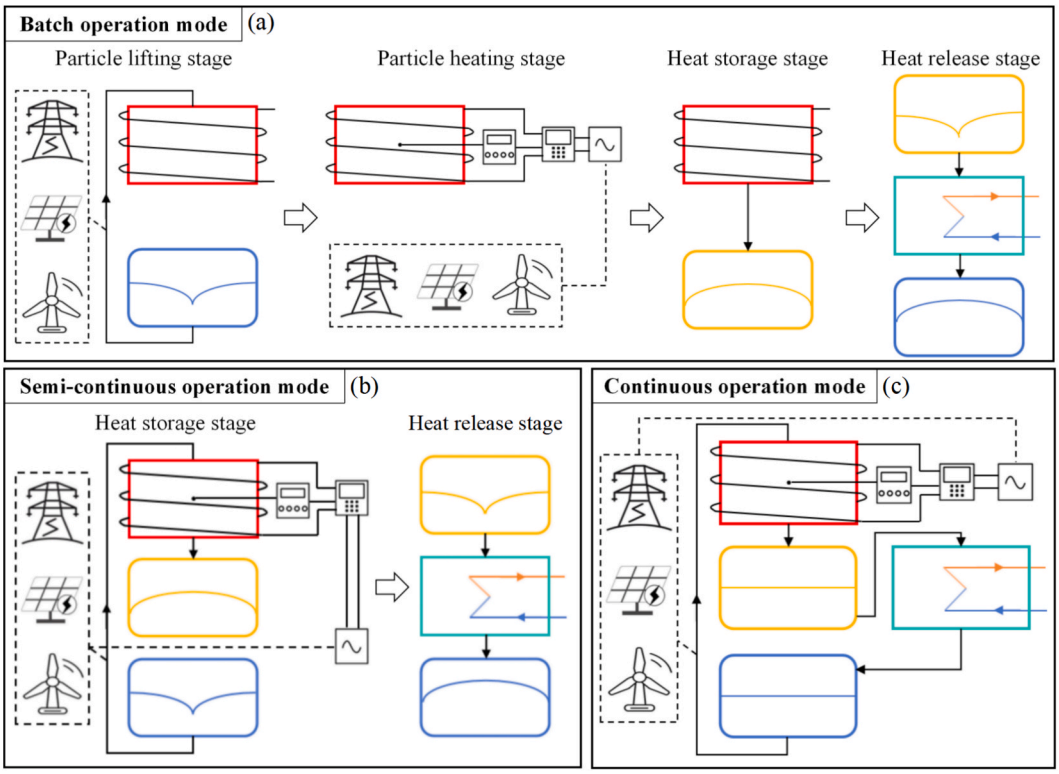

Fig. 2. Diagrams of systematic operation modes, including a) batch operation mode, b) semi-continuous mode, and c) continuous operation mode.

storage. Finally, if there is a demand for electricity, the fourth stage activates, prompting the particles to release their sensible heat. Subsequently, the particles are introduced into the cold bulk storage unit, where they await the next turn.

It can be concluded that the batch operation mode is suitable for scenarios where heat storage and release occur over a relatively short period (usually less than one hour), as each batch of steel pellets has a finite amount of heat available. This mode offers a flexible control mechanism and facilitates straightforward start-up and shutdown procedures. For instance, if a significant surge in wind power generation is anticipated in the near future, the batch operation mode can effectively convert the excess electricity generation into thermal energy for storage and provide temporary power generation when wind power input is insufficient.

(2) The semi-continuous operation mode only has two stages, which are heat storage stage and heat release stage. The heat storage stage works in a continuous mode, where particles are persistently delivered from the cold bulk storage unit into the hot bulk storage unit. Following this stage, the particles have accumulated a significant amount of heat energy and can further release it if needed during the subsequent heat release stage. The primary distinction between the batch operation mode and the semi-continuous mode lies in the fact that in the former, the heated particles remain nearly stationary, whereas in the latter, the particles are in constant motion due to gravity. Furthermore, there is no specific differentiation between the sources of electrical energy that the two modes can utilize.

This mode is anticipated to be the most commonly utilized due to its applicability to solving time-domain mismatches between electricity production and consumption over a longer period (usually longer than 4 h). For instance, it is appropriate to store a certain amount of solar energy in the form of thermal energy during the day. This helps mitigate the inherent volatility and instability of solar energy and prevents power shortfalls at night by releasing the absorbed thermal energy as electricity.

(3) The continuous operation mode refers to an operation approach of continuously consuming surplus electricity with a stable heat output. In this mode, all the equipment is in a stable operating state at the same time. This mode is well-suited for cogeneration units, and the integration of the ETES system effectively ensures thermoelectric decoupling, allowing excess electricity (beyond grid demand) to be converted into heat storage and supplied on demand. This mode is suitable for heat-supplying scenarios characterized by long duration, extensive coverage, and high demand. However, it should be noted that the overall efficiency of this system is lower than that of conventional electric boilers due to the inevitable heat transfer loss. In this work, this operation mode is not further considered here, as it does not involve electricity regeneration.

2.2. Material and parameter consideration

2.2.1. Materials

In an EIHS-MBHR system, the appropriate selections of several critical materials are essential to ensure safe and stable operation, including but not limited to particle material, EI heater base material, and electromagnetic shield material.

A high melting point coupled with a low Curie point or weak magnetism ensures that the particles can flow smoothly in the system without particle sintering and particle clogging. The austenitic stainless steel is a suitable selection. In addition to above consideration, such material also offers numerous advantages over alternative options (silica sand, molten salt, etc.). For example, the thermal conductivity of austenitic stainless steel is approximately 20 W/m/K at room temperature, significantly higher than that of silica sand (~0.6 W/m/K) and molten salt (~1 W/m/K), leading to more intense heat transfer, a faster rate for heat release, and a faster load response. Furthermore, the austenitic stainless steel, storing heat as sensible heat, allow a wider operation temperature range with a higher upper limit. As a comparison, molten salts are typically operated within a relatively narrow temperature range, such as [290,560] ℃ for solar salt [39], in order to maintain fluidity and thermal stability while preventing corrosion of metal tubes.

In order to achieve direct heating of conductive particles and avoid electromagnetic shielding effect, the EI heater base material should possess adequate structural strength, high temperature resistance, low thermal conductivity, and be non-conductive electrically, for example insulating ceramics.

The electromagnetic shield is set for confining the magnetic field to the inside EI heater body, thereby reducing magnetic leakage, preventing external metal components from being heated, and avoiding unnecessary energy loss. However, due to the Joule's effect, the EI coils are plagued by high temperature operating environment even if its electric resistance is quite low, leading to the need of forced-cooled radiators (e.g. air-cooled radiator) to ensure the safe and stable operation. Following this requirement, the electromagnetic shield is suggested to be made of metal dense mesh constructed by copper, enabling the smooth passage of cooling air.

2.2.2. Geometric parameters

Considering the ease of installation and convenient feeding and discharging of particles, the rectangular cross-section design is adopted for the hot bulk storage, the cold bulk storage, and the tubular MBHE. Furthermore, the EI heater employs the same design to facilitate its structural integration and to ensure the effective utilization of the limited space. However, it should be noted that the circular cross-section design for EI heater generally offer better heating uniformity and straightforward coil winding process compared to the rectangular cross-section, which often make it also a readily acceptable solution in many cases. Note that the inappropriate cross-sectional sizes of the EI heater can degrade the heating uniformity under specified operating conditions due to the skin effect [40], leading to an inherent issue: the sizes of the EI heater cannot be indefinitely increased. This issue can further limit the engineering applications of this system as a large enough EI heater is required in industries. A possible solution to this issue is come up with and described detailly in Section 2.3.

The number of turns in the EI coils mainly affects the particle heating power. As increasing the number of turns, the magnetic field intensity within the heater is amplified, resulting in stronger induced eddy currents within the particles. However, increasing the number of turns leads to greater heat generation by the coils themselves, which may fail to meet operation requirements. Hence, it is recommended to adopt a reasonable number of turns considering the actual device scale.

The dimensions of the hot and cold bulk storage units can be determined by the total mass of circulating particles. While, the dimensions of the tubular MBHE are depended on the heat transfer conditions, such as inlet particle temperature and outlet steam temperature.

Particle diameter is another key geometric parameter that needs careful consideration. As reported in literature [41–43], the volume density of the power absorbed by a single particle (W_H/V, the detailed expression is presented in Section 3.1.1) lies on the ratio of particle diameter to skin thickness (d_p/δ_s) when other operation parameters are determined. In this paper, this ratio is set to a value between 4.8 and 5, and a satisfactory particle heating effect can be attained [41–43].

2.2.3. System operation parameters

Regarding the operation parameters, there are several different types due to the inherent complexity of the EIHS-MBHR system, such as parameters of EI heating, particle-side operation, and fluid-side operation. Generally, it is suggested to consider the specific requirements comprehensively and then determine the parameter selections carefully. For instance, only through comprehensive selection of particle diameter and inverter can we effectively determine the heating frequency f, a critical parameter for EI heating.

Additionally, particle-side operation parameters mainly consist of particle mass flow in the EI heater (only valid for semi-continuous and continuous mode) and tubular MBHE, as well as particle temperatures in hot and cold bulk storage units while fluid-side parameters primarily include inlet water temperature and pressure, outlet water temperature and pressure, and outlet steam mass flow. Upon selection of the steam turbine, these fluid-side parameters can be primarily established based on the turbine's operation requirements. Subsequently, according to the traditional design approach of heat exchangers, the particle-side inlet and outlet temperatures, which respectively correspond to the particle temperature in hot bulk storage unit and the particle temperatures in cold bulk storage unit, can be determined by estimating the heat transfer temperature differences at the hot and cold ends of the heat exchanger. Furthermore, based on the principle of energy conservation, the mass flow rate of particles and total heat transfer area required in the tubular MBHE can be ascertained roughly. Besides, the dimensions of the tubular MBHE can also be determined once the total heat transfer area has been specified. Therefore, all the operation parameters mentioned above can be reasonably confirmed.

2.3. Engineering application

For a better understanding, a potential engineering application scheme of the EIHS-MBHR system is proposed and illustrated here. This engineering application encompasses all the components detailed above, featuring the EI heater as highlighted in Fig. 3, including a particle distributor, a ceramic lining, a particle collector, and several electromagnetic shielding enclosures (marked with blue dashed boxes). To realize EI coil forced cooling, an inlet and an outlet of air flow are installed on the ceramic lining. In order to deal with the difficulty of EI heaters for scaling up, it can be considered that each basic unit is a small size EI heater, enveloped by a thermal insulating layer, an EI coil, and an electromagnetic shielding enclosure (as shown in Fig. 3).

Some parameters of this potential engineering application are listed in Table 1 and Table S1, Supplementary Material (SM), involving material parameters, EI heater parameters, tubular MBHE parameters, steam turbine operating parameters, and generator operating parameters. Note that the temperature differences for heat transfer at the hot end and cold end are set to 280 ℃ and 130 ℃, respectively, thus the inlet and outlet particle temperatures of the EI heater can be ascertained accordingly. In addition, some key parameters, including EI heating efficiency η_{Elh}, heat utilization efficiency in the tubular MBHE η_{hu}, actual power coefficient η_{ap}, and power generation efficiency η_{pg}, are determined based on engineering experience (see Table S1). In this engineering application, the target scale of ETES capacity is equivalent to EI heating power.

3. Theoretical analysis methods

3.1. Thermal analysis

3.1.1. Model description

The CFD-DEM model used in this paper is developed based on our previous work [35], with specific model descriptions available therein. For simplicity, only the key governing equations are listed for reference, as presented in Table S2.

To simplify the calculation, it can be assumed that the EI heating effect equivalently provides an internal heat source to each particle, and the internal heat source strength (W_H) in each particle is uniform due to the homogeneity of EI heating [21–26], as written in Eq. (1).

$$m_p C_{pp} \frac{dT_p}{dt} = \sum Q_{px} + W_H \tag{1}$$

where m_p refers to the particle mass, C_{pp} the particle specific heat capacity, T_p the particle temperature, t the time, and Q_{px} the particle heat flux involving conduction, convection, and radiation.

The key lies in directly calculating the intensity of the W_H without additional electromagnetic simulation. Tanabe [41] utilized the Mie theory to describe the power absorbed by a single spherical particle under irradiation from a plane electromagnetic wave, deriving a

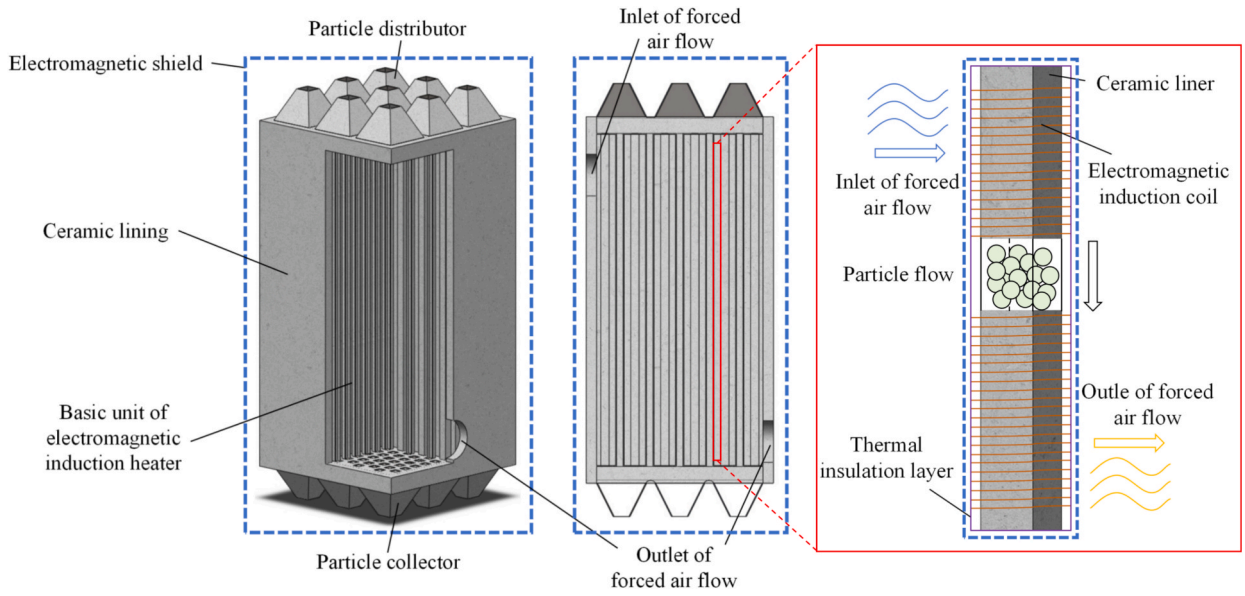

Fig. 3. A preliminary design scheme of the EI heater in the EIHS-MBHR system.

Table 1
Key parameters of a potential engineering application.

Material parameters			
Particle material	Stainless steel 304	Particle diameter d_p (mm)	8, selected according to δ_s
Shell material of EI heater	Alumina ceramics	Tube material	Steel 20G
EI heater parameters			
Inlet particle temperature (℃)	150.0, specified	Outlet particle temperature (℃)	800.0, specified
Skin thickness δ_s (mm)	1.64, Eq. (S1)	EI heating power P_{EIh} (kW)	7330, Eq. (S2)
Tubular MBHE parameters			
Inlet particle temperature (℃)	800.0, specified	Outlet particle temperature (℃)	150.0, specified
Rated mass flow rate of particles $\dot{m}_p$ (t/h)	51.3, Eq. (S3)	Inlet water temperature (℃)	20.0, specified
Inlet water absolute pressure (MPa)	12.1, specified	Outlet steam temperature (℃)	520.0, specified
Outlet steam absolute pressure (MPa)	12.1, specified	Rated mass flow rate of outlet steam $\dot{m}_s$ (t/h)	~6.1, Eq. (S4)
Steam turbine operating parameters (Siemens D-R C type)			
Inlet steam temperature (℃)	520.0, determined by the steam turbine	Inlet steam absolute pressure (MPa)	12.1, determined by the steam turbine
Rated mass flow rate of inlet steam $\dot{m}_s$ (t/h)	~6.1, Eq. (S4)	Actual steam turbine output P_{ao} (kW)	2375, Eq. (S5)
Generator operating parameter			
Generator output P_{go} (kW)	2256, Eq. (S6)		

corresponding mathematical expression to numerically determine W_H (see Eq. (2) to Eq. (4)).

$$W_H = \frac{36\pi f B_0^2}{\mu_m}\left(\frac{\delta_s}{d_p}\right)^2\left[\frac{d_p}{2\delta_s}\frac{\sinh(d_p/\delta_s)+\sin(d_p/\delta_s)}{\cosh(d_p/\delta_s)-\cos(d_p/\delta_s)}-1\right] \quad (2)$$

$$B_0 = \frac{\mu_m T_c I_c}{h_c K} \quad (3)$$

$$K = 1 + 0.44 D_c/h_c \quad (4)$$

where B_0 refers to the amplitude of the incident magnetic flux density, K the correction coefficient, T_c the turns per coil, I_c the coil maximum current, h_c the coil height, and D_c the coil inner diameter. Eq. (3) and Eq. (4) are originated from Ref. [44].

The main assumptions of Eq. (2) are as follows [41]:

(1) The classical Mie theory is satisfied under the following conditions: a single spherical particle is irradiated by a plane electromagnetic wave. This implies that the equation may suffer from distortions when describing the behavior of particle groups, particularly for irregularly shaped particles;
(2) The particle is nonmagnetic and metallic, with its center positioned at the maximum of the magnetic field. This latter condition constitutes a strong simplifying assumption for reducing the complexity of the general analytical solution to Maxwell's equations;
(3) The size of the particle is sufficiently smaller than the wavelength of the electromagnetic field. This condition can generally be satisfied in most practical scenarios, except when the heating frequency is sufficiently high, such as in the GHz range.

Actually, according to the study of Ignatenko et al. [45], the calculation of W_H for a single particle in an isolated system is significantly differs from that in a clustered system comprised of numerous particles. They found that the average W_H of multiparticles is slightly lower than that of a single particle. They concluded that the induced currents within each particle can interact with those of neighboring particles, and these particles are not subjected to irradiation by plane waves, but rather by a superposition of incoming and scattered waves from other particles. In contrast, it is mentioned by Lu and Zhang [46] that in an alternating magnetic field, due to the stacking of conductive particles, the cumulative amplitude of the superposition field may exceed the amplitude of the original activation field at each particle location, leading to rapid boiling of interstitial water and bulk sintering of metal particles.

Given these, it seems that there remains a research gap in quantitatively modeling electromagnetic induction heating for multi-particle systems. Therefore, this study adopts the simplified single-particle EI heating model (Eq. (2)) as the computational baseline. The practical applicability of this sub-model is questionable in the absence of any verification or correction, as it may introduce scenario-dependent prediction biases in W_H by overestimating or underestimating certain

factors. To address this limitation, the CFD-DEM with an EI heating sub-module is subjected to systematic quantitative validation through comparative analysis with experimental datasets, as detailed in Section 4.1..

3.1.2. Simulation conditions

According to Section 2.3, an EI heater unit and a tubular MBHE unit are modeled and utilized for conducting CFD-DEM simulations after being meshed (see Fig. 4 for details). It is suggested that the average ratio of mesh size to particle size in CFD-DEM simulation should be controlled within the range from 3 to 10 [47]. While, due to the use of the node-based averaging of the discrete phase quantities in CFD module, the lower constraint on the average ratio of mesh size to particle size can be suitably relaxed [48]. Therefore, these ratios of the heater and heat exchanger are respectively set to 2.2 and 1.6 for subsequent simulations.

SRK equations, as well as the temperature-dependent parameters of air involving heat conductivity, specific heat capacity, and viscosity, are adopted based on our previous studies [35,49]. To align with actual operations, the EI heater and the tubular MBHE lack inlets and outlets for the interstitial fluid, resulting in natural convection within these units. In more details, all walls are treated as adiabatic, and the inlet particle temperature is set to 300.0 K in the EI heater. The particle heating process is detailly captured in this study. In the tubular MBHE, all walls except the tube walls are considered adiabatic, and the tube wall temperatures are assumed to be constant. It should be noted that both the particle and tube wall temperatures are set to their respective averages, in order to obtain the average heat transfer coefficient in the tubular MBHE. The wall temperature is calculated by averaging the water-side inlet and outlet temperatures, with the assumption that the wall temperature is close to the fluid medium flowing inside (refer to Table 1). Meanwhile, the particle inlet temperature used in this study is the average of the preset particle-side temperatures at the outlet and inlet (refer to Table 1), and the particle temperature remain unchanged during the simulation. With these settings, representative heat transfer results in tubular MBHE can be achieved without expending significant computational resources.

Some main parameters are detailed in Table 2. For simplicity, other settings of models and parameters, such as numerical methods, remain consistent with our previous studies [35,49].

Table 2
The list of parameters used in simulations.

Name		Value	Unit
Material roughness	Particle	2.5×10^{-6}	m
	Tube	2.5×10^{-6}	m
Emissivity	Particle	0.8	/
	Tube	0.8	/
Particle-to-wall contact and particle-to-particle contact [50]	Coefficient of restitution	0.7	/
	Coefficient of static friction	0.2	/
	Coefficient of rolling friction	0.01	/
Gas film thickness		0.8	mm
Air pressure		1	atm
EI heater unit	Air initial temperature	26.85	℃
	Inlet particle temperature	26.85	℃
	Particle descending velocity	2	mm/s
	Time step in EDEM	5×10^{-5}	s
	Time step in Fluent	1×10^{-3}	s
Tubular MBHE unit	Air initial temperature	270	℃
	Inlet particle temperature	475	℃
	Tube wall temperature	270	℃
	Particle descending velocity	2	mm/s
	Time step in EDEM	5×10^{-5}	s
	Time step in Fluent	5×10^{-3}	s

3.2. Economic analysis

3.2.1. Model description

There are at least two business models applicable to the project mentioned in Section 2.3, named as business models 1 and 2. The business model 1 utilizes valley power to supply peak power demands, whereas model 2 uses abandoned photovoltaic and wind power. The economics of these two business models are numerically modeled here.

As depicted in Eq. (5), the annual total operating revenue consists of three parts: the benefit for the supply of peak electricity Y_{pe}, the comprehensive subsidy for the supply of peak electricity Y_{cs}, and the

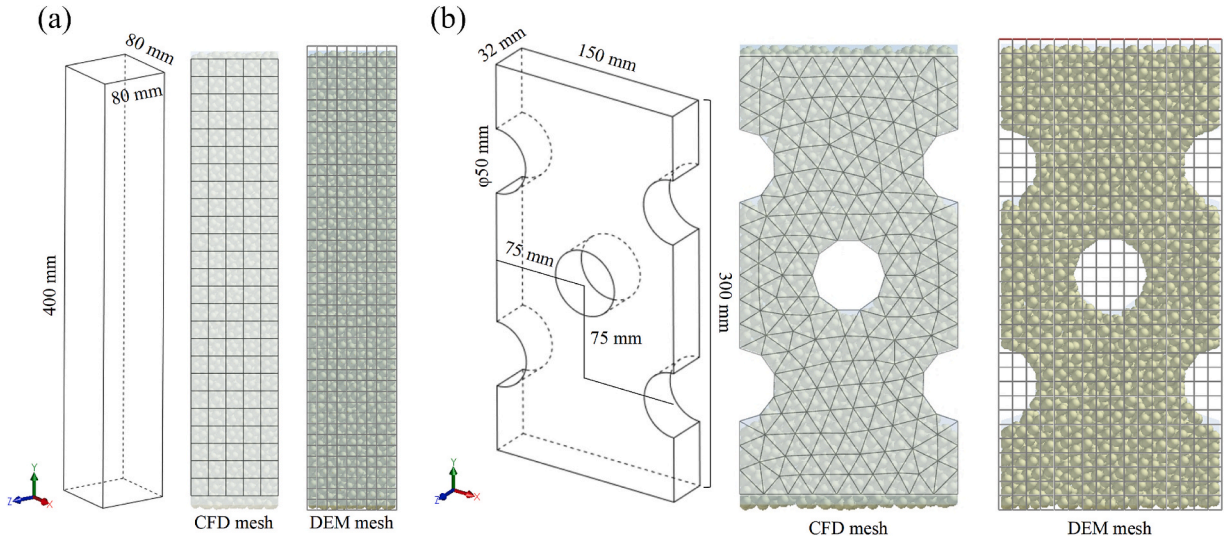

Fig. 4. Geometries and meshes of an EI heater unit and a tubular MBHE unit. There are 640 CFD grids and 2112 DEM grids for the heat exchanger, along with 625 CFD grids and 3483 DEM grids for the heater.

additional government subsidy for the project Y_{gs}.

$$Y_{op} = Y_{pe} + Y_{cs} + Y_{gs} \tag{5}$$

Generally, the main revenue comes from Y_{pe}, which corresponds to the heat release stage of the semi-continuous operating mode:

$$Y_{pe} = P_{rp}(1 - r_{scp}r_{pp})e_p h_{hr} \tag{6}$$

where r_{scp} is the ratio of the self-consumption power to P_{rp} (rated power of steam turbine), r_{pp} the ratio of the peak power demand for self-consumption to the self-consumption power, e_p the price of peak electricity, and h_{hr} the annual operation hours for heat release.

Eq. (7) presents the expression of Y_{cs}, which is mainly derived from the provision of power services, including energy storage and peak shaving, as well as offering eco-compensation, such as carbon emission reduction. Actually, quantifying these subsidies individually poses a challenge, hence a pre-assumed value, the comprehensive subsidy per kW·h for the supply of peak electricity e_{cs}, is used to collectively characterize them. Similarly, Y_{gs}, which reflects the government's support for the project, is assumed to be constant and is provided annually.

$$Y_{cs} = P_{rp}(1 - r_{scp}r_{pp})e_{cs}h_{hr} \tag{7}$$

Meanwhile, the annual total operating cost comprises 6 parts: the operating cost of using valley electricity to meet the self-use requirements C_{ve}, the operating cost of EI heating C_{EIh}, the operating cost of hiring workers C_{hw}, the operating cost for equipment maintenance C_{em}, the operating cost for supplement water supply C_{sw}, and the operating cost of supplement particle supply C_{sp}, as expressed in Eq. (8):

$$C_{op} = C_{ve} + C_{EIh} + C_{hw} + C_{em} + C_{sw} + C_{sp} \tag{8}$$

The operation costs can be obtained as shown in Eqs. (9)–(14). For business model 2, due to the fact that the electricity consumption comes from the abandoned photovoltaic and wind power, which are considered as free, the operating cost of using valley electricity to meet the self-use requirements C_{ve} (see Eq. (9)) and the operating cost of EI heating C_{EIh} are considered to be zero (see Eq. (10)).

$$C_{ve} = B_m \times [P_{rp}r_{scp}(1 - r_{pp})e_v h_{hs}],\ B_m = \begin{cases} 1, & \text{for business mode 1} \\ 0, & \text{for business mode 2} \end{cases} \tag{9}$$

$$C_{EIh} = B_m \times P_{EIh}e_v h_{hs} \tag{10}$$

$$C_{hw} = w_s n_w \tag{11}$$

$$C_{em} = I_e \cdot \eta_{em} \tag{12}$$

$$C_{sw} = \dot{m}_{sw}h_{hr}p_w \tag{13}$$

$$C_{sp} = \dot{m}_{sp}p_p \tag{14}$$

where B_m represents the coefficient related to business models, e_v the price of valley electricity, w_s the average salary of a single worker per year, n_w the number of workers, I_e the total investment, η_{em} the equipment maintenance factor, $\dot{m}_{sw}$ the mass flow rate of supplement water per hour, p_w the price of supplement water, $\dot{m}_{sp}$ the mass flow rate of supplement particles, and p_p the price of supplement particles.

Hence the annual net profit, Y_{net}, can be calculated as Eq. (15).

$$Y_{net} = Y_{op,\,i} - C_{op,\,j} \tag{15}$$

Subsequently, according to definition of net present value (*NPV*, see Eq. (16)), two crucial parameters can be further obtained: the payback period *PBP* (a minimum number of years n_{min} meeting $NPV \geq 0$ with a set interest rate r) and the internal rate of return (*IRR*) (a specific r meeting $NPV = 0$ with n adopting the project life cycle L_c).

$$NPV = \sum_{x=0}^{n} \frac{M_x}{(1+r)^x},\ M_x = \{Y_{net,\,0} = -I_t, Y_{net,\,1}, Y_{net,\,2}, \ldots, Y_{net,\,x}\} \tag{16}$$

where M_x is the money flow over x years.

In addition, the impacts of several critical parameters (*Fij*) in this evaluation model on the *IRR* are explored through a sensitivity analysis, with the change ratios set to ± 20 % and ± 10 % (see Eq. (17) and Eq. (18)).

$$S_{ij,z} = \frac{(IRR_{ij,z} - IRR_{base})/IRR_{base}}{(Fij_z - F_{base})/F_{base}} \tag{17}$$

$$\overline{S_{ij}} = \frac{\sum_{z=1}^{4} S_{ij,z}}{4} \tag{18}$$

where S_{ij} is the sensitivity coefficient of factor *Fij* and $\overline{S_{ij}}$ is the average sensitivity coefficient of multiple tests.

3.2.2. Parameter settings

In this work, it is suggested that I_t mainly includes the equipment cost I_e, the cost of equipment installation I_{ei}, the land cost I_l, the cost of project design I_{pd}, the engineering test cost I_{et}, project management cost I_{pm}, as illustrated in Eq. (19). I_e and I_{ei} are determined based on engineering experience, as detailed in Table S3.

$$I_t = I_e + I_{ei} + I_l + I_{pd} + I_{et} + I_{pm} \tag{19}$$

Other model parameters are artificially estimated, as shown in Table 3. The evaluations of these parameters primarily refer to current situation of investment market and electricity market to ensure their authenticity and representativeness.

4. Results and discussions

4.1. Model validation

Herein, a temperature rise experiment conducted by Deng [27] on a steel pellet fixed bed with interstitial air is used to validate the model's accuracy. Detailed information of this experimental system (Fig. S2), as well as the experimental procedure and conditions (Table S4), can refer to Ref. [23,27] or the attached SM.

The temperature rise rates of particles and interstitial fluid are shown

Table 3
Parameters used in economic analysis.

Parameter	Value	Unit
P_{go}	2256, see Table 1	kW
Y_{gs}	100.0	$\times 10^4$ ¥/y
r_{sp}	0.05	/
r_{pp}	0.2	/
e_p	1.3	¥/kW·h
h_{hs}	2920, for business model 1	h/y
	880, for business model 2	h/y
h_{hr}	2920, for business model 1	h/y
	880, for business model 2	h/y
e_{cs}	1.0	¥/kW·h
e_v	0.3	¥/kW·h
$\dot{m}_p$	14.26, see Table 1	kg/s
$\Delta\varphi_p$	488.5, see Table S1	kJ/kg
η_{EIh}	0.95	/
w_s	20.0	$\times 10^4$ ¥/y
n_w	5	/
η_{em}	0.01	/
$\dot{m}_{sw}$	1.0	t/h
p_w	8.0	¥/t
$\dot{m}_{sp}$	2.0	t/y
p_p	2.0	$\times 10^4$ ¥/t
L_c	30	y
I_l	500.0	$\times 10^4$ ¥
I_{pd}	100.0	$\times 10^4$ ¥
I_{et}	50.0	$\times 10^4$ ¥
I_{pm}	50.0	$\times 10^4$ ¥
$I_{t,\,k}$	4012.0	$\times 10^4$ ¥

in Fig. S3. It's worth noting that a non-uniform distribution of temperature rise rates is observed, particularly at the two ends of the experimental segment. In addition, Meng et al. [23] also reported this unique phenomenon and attributed it to the scattering of magnetic field lines at both ends of the heater. This scattering results in an edge effect, thereby causing the magnetic field strength to be weaker at the edges compared to the middle. The magnetic scattering phenomenon can be virtually eliminated by ensuring that the heating section has a sufficiently large height-to-diameter aspect ratio.

In this study, data from the middle section (refer to Fig. S3, position: P4–P12), rather than the edges, are utilized to determine the experimental value of $W_{H,exp}$, as estimated by Eq. (20). Given this, a similar fixed bed system is established to obtain $W_{H,sim}$ by Eq. (20) from a CFD-DEM simulation perspective, in order to ensure the comparability of the results. The final comparison results are depicted in Table 4. The heating performance of a packed bed with air as the interstitial fluid is slightly weaker compared to a packed bed with water as the interstitial fluid, even when the total input power remains constant. Deng argued that this discrepancy occurs because water, as the interstitial fluid, can enhance the magnetic permeability of the surrounding medium, especially when the bed contains oxidized stainless steel particles [27]. Overall, the simulation results demonstrate a satisfactory level of accuracy when compared to the experimental data, as the relative errors remain below 10 %. Hence, it can be considered that our CFD-DEM model integrated with an EI heating sub-model is relatively effective and accurate.

$$\begin{cases} W_{H,exp/sim} = C_{pp} m_p \dfrac{\overline{\Delta T_p}}{\Delta t} + C_{pf} m_f \dfrac{\overline{\Delta T_f}}{\Delta t} m_p = \dfrac{\pi \rho_p d_p^3}{6} m_f = \dfrac{\rho_f \pi d_p^3 \alpha_f}{6(1-\alpha_f)} \end{cases} \quad (20)$$

where C_{pp} refers to the particle specific heat capacity, C_{pf} the fluid specific heat capacity, m_f the mass of the surrounding fluid, $\frac{\overline{\Delta T_p}}{\Delta t}/\frac{\overline{\Delta T_f}}{\Delta t}$ the average temperature rise rate of a single particle or the surrounding fluid, ρ_p/ρ_f the particle/fluid density, and α_f the packed bed porosity.

4.2. Particle heating process in EI heater

In the EI heater unit, particles are expected to descend smoothly under the influence of gravity and the solid flow controller for discharge, such as screw discharging machine, and to be gradually heated to a preset temperature. Thus, it is essential to investigate the particle flow characteristics and the particle temperature distributions along both the axial and radial directions in the EI heater unit to further reveal the comprehensive performance in EI heater. In general, it can be considered that the particle flow within the unit exhibit a plug or integral flow behavior, as evidenced by the uniform downward movement of particles without any significant lateral transfer. It should be noted that, due to the effect of particle–wall friction and the actually uneven downward process of the particles, the particle velocity is unevenly distributed in space, which is shown in Fig. S4. However, the degree of non-uniformity in the velocity distribution within our studied operation conditions is relatively small, therefore, the particle flow pattern can still be approximately regarded as plug flow. The particle temperature distribution at a simulation time of 100 s (see Fig. 5a) is relatively uniform along the X-axis with no obvious tilted temperature layer. This result can further illustrate the existence of a plug or integral flow.

Distinct temperature gradients are also observed in Fig. 5a along the Y-axis at the upper section of the unit, with a maximum temperature increase of approximately 334 K. However, there is an even temperature distribution in the lower part, which can be attributed to the insufficient simulation time. Predictably, this uniform temperature distribution is expected to gradually disappear with the extension of simulation time (at least 200 s, an estimated time to exclude all initial particles), however, this necessitates substantial computational resources. Actually, the particle flow can reach a stable state through a short time (~10 s) according to our simulation, therefore, a compromise method is adopted herein which can predict the temperature distribution after stabilization in a limited calculation time, rather than simulating for an extended period to directly obtain the temperature distribution.

From Fig. 5b, four sets of data are extracted to quantitatively characterize the temperature distributions at the respective four simulation times. Overall, a single temperature distribution curve in Fig. 5b can be divided into three stages, which are the stable stage, the transition stage, and the linear stage:

(a) In the linear stage, newly added particles experience strong heating due to the EI effect and gradually move downward (the Y coordinate value decreases), as residence time extends. The slope of this linear stage mainly depends on the strength of EI effect, and this linear stage is heating-dependent.
(b) Particles operating in the stable stage are the original ones that remain in the system without being fully excluded. They are continuously heated throughout the simulation, resulting in a relatively consistent temperature distribution. From this perspective, this stable stage is also heating-dependent.
(c) In the transition stage, the temperature distribution undergoes a transition from a linear increase to a stable state. In essence, the particles in this state include new added ones and initial ones, which are affected by both the EI effect and the heat transfer effect. Due to the latter effect, particles in the stable stage, which exhibit higher temperatures, tend to transfer heat to those in the linear stage, facilitating a smooth transition. Thus, the transition stage is heating-dependent and transfer-dependent. However, given sufficient simulation time, the stable stage and the transition stage tend to disappear.

It can be seen from Fig. 5b that the linear stage exhibits the same slope regardless of the simulation time. These suggest that a predicted temperature distribution of the system in the final stable state can be obtained. The fitting result can also be found in Fig. 5b with the R-squared (R^2) of 0.9993. From this relationship, the final outlet particle temperature can be calculated to be 724.54 ℃. Besides, a theoretical outlet particle temperature can also be obtained based on the particle residence time (~200 s) and average temperature rise rate (3.33 K/s, see Fig. 5b), which is 692.85 ℃. The relative error is less than 4.6 %, indicating the relative accuracy of the trend prediction. Based on it, it is possible to anticipate the particle temperature at the exit of a real unit by generalizing the linear heating phenomenon, which is crucial for the particle temperature control.

There are two key parameters for particle heating stage and subsequent heat storage stage: temperature rise rate and particle heat storage density. In this case, the average temperature rise rate is 3.33 K/s, indicating that a strong EI heating effect exists. It is noteworthy that the actual particle temperature rise rate can be tailored to meet specific particle heating requirements by adjusting parameters such as the number of coil turns, the coil height, the operating frequency, and the current magnitude in the coil. However, it is crucial to carefully regulate this rate to avoid damaging the base material or particle material due to excessive thermal stress, while also ensuring that the surplus power is effectively utilized within a limited timeframe. Subsequently, the

Table 4
Comparison results.

Interstitial fluid	$W_{H,sim}$(W)	$W_{H,exp}$(W)	Relative error (%)
Air	1.95779×10^{-2}	1.78590×10^{-2}	9.62
Water	1.95780×10^{-2}	2.16032×10^{-2}	9.37

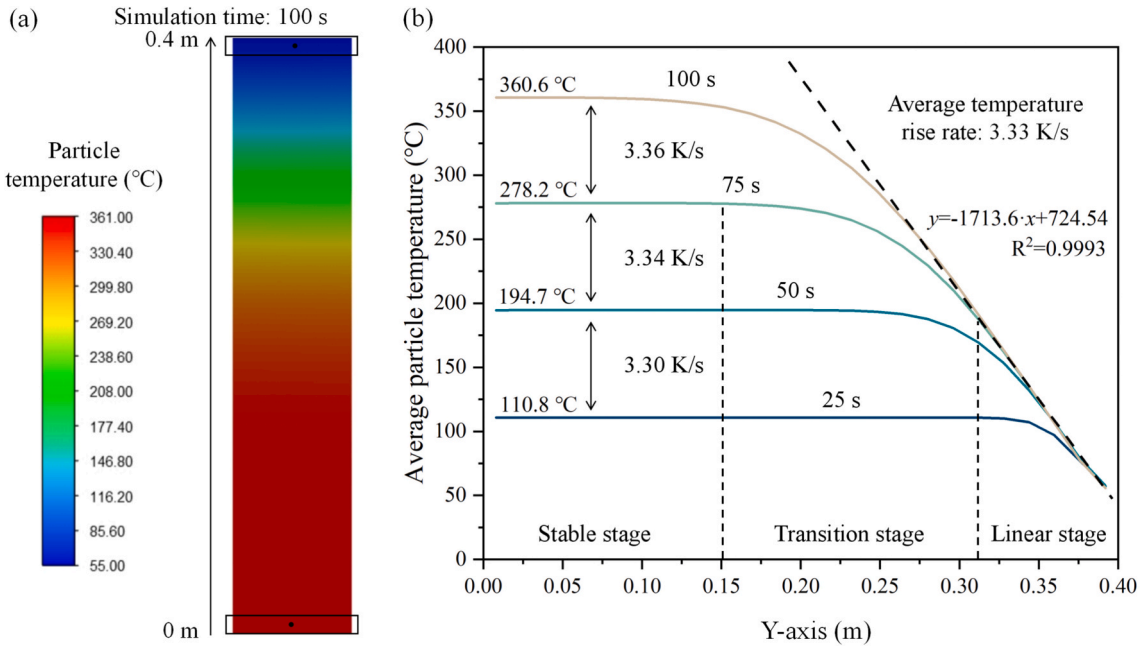

Fig. 5. The diagrams of a) the distribution of particle temperature along Y-axis at simulation time of 100 s and b) the relationships between average particle temperature and Y-axis position at various simulation times.

thermal storage density is determined by the specific heat capacity of particle materials and the temperature differential during heat storage and release. Assuming a particle specific thermal capacity of 700 J/kg/K and a temperature increase of 700 K, the particle heat storage density is calculated to be 490 kJ/kg. The temperature increase in the EI heater is likely to be greater than that in a Joule heater, as the heating temperature in a Joule heater is constrained by the high-temperature tolerance of the heating resistor and the inherent heat transfer temperature difference between the hot surface and the cold particles. However, given the same temperature difference, the thermal storage density of stainless steel particles is about half that of silica sand (~1000 kJ/kg) due to its smaller specific heat capacity, which is determined by the material itself. Although stainless steel particles are inferior to silica sand in terms of thermal storage density, their excellent thermal conductivity (generally an order of magnitude higher than that of silica sand) makes them significantly better at maintaining a higher heat release rate in the system. Given these, it is considered that stainless steel particles, when used as heat storage media, possess a suitable heat storage density and show promising potential for various applications.

In summary, the EI heater offers a uniform heating effect and an adjustable heating rate when using stainless steel particles, which also exhibit a satisfactory thermal storage density.

4.3. Heat release performance in tubular MBHE

In the tubular MBHE unit, five tubes are embedded, each labeled with serial numbers from 1 to 5, as shown in Fig. 6. It can be seen in Fig. 6a that the particles are dense packed with less void zone below tubes due to the large ratio of tube diameter to particle diameter (50/8 = 6.25). During the operation, the particle flow presents a semi-integral mode as particles near the tube are hindered and slightly packed on top of the tube, as demonstrated in Fig. 6b. This stagnation phenomenon causes that the updating rate of particles near the tube is relatively slow, which may be not conducive to heat transfer [51,52]. Furthermore, from Fig. 6c, there are several void zones existing beneath the tube, characterized by a high air volume fraction, which may also hinder heat transfer [52,53]. Due to the heat transfer between air and tube wall, the air temperature is lower near the tube and more evenly distributed elsewhere.

For further analyzing the heat transfer intensity, heat transfer co-

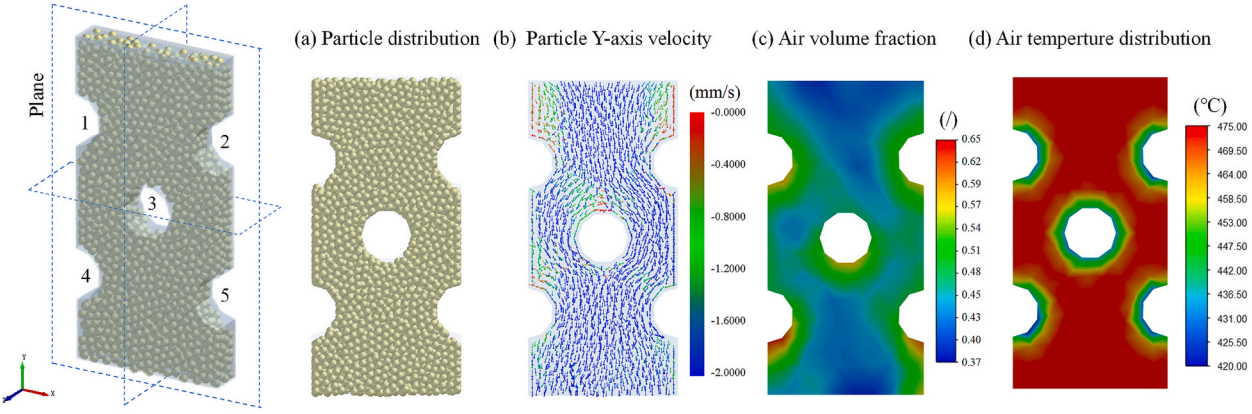

Fig. 6. Distributions of a) particle location, b) particle Y-axis velocity, c) air volume fraction, and d) air temperature within the tubular MBHE unit, at the simulation time of 17.8 s.

efficients h_{coef} of different tubes are employed, as calculated by Eqs. (21) and (22). It's worth mentioning that these values mainly reflect the average heat transfer intensity within the tubular MBHE, as they are based on the boundary conditions averaged from the operation conditions of the potential engineering application.

$$h_{coef,\,i} = \frac{Q_{w,\,i}}{Area_i \times \Delta T_{p-w}},\ i = 1,\ 2...,5 \tag{21}$$

$$Q_{w,\,i} = Q_{p-w,\,i} + Q_{f-w,\,i} \tag{22}$$

where i is the tube serial number, Q_w the heat flux received by tube wall (including the particle-to-wall heat flux Q_{p-w} and the fluid-to-wall heat flux $Q_{f-w,}$), *Area* the heat transfer area, and ΔT_{p-w} the particle-to-wall temperature difference.

Taking tube 3 as an example, as shown in Fig. 7a, h_{coef} usually changes with simulation time; thus, an average value over the last 5 s is adopted to ensure the representativeness. Given this, the average heat transfer coefficients of tubes 1–5 can be obtained and presented in Fig. 7b. However, the heat transfer coefficients of different tubes show certain deviations due to the fact that their particle surround conditions are varying (see Fig. 7c). Due to the interactions between tubes arranged vertically [49], the heat transfer intensity of the upper row of tubes is higher than that of the lower row of tubes, which is also true in the case of staggered tubes as heat transfer coefficients of tubes 1–3 are slightly higher than those of tubes 4 and 5.

It can be seen that h_{coef} is ranging from 678.2 W/m^2/K to 784.6 W/m^2/K, which is relatively higher than that of traditional tubular MBHEs [36]. This highlights the unit's satisfactory heat release performance, attributed to the high thermal conductivity of the particle materials, indicating that this heat release equipment is well-suited for timely supply of peak power. What's more, the higher heat transfer coefficient can result in less heat transfer area required under given operation conditions, further leading to lower equipment investment of this heat exchanger.

4.4. Economic analysis of EIHS-MBHR system

4.4.1. Systematic economic evaluation

From Section 2.3, it can be found that for this possible application, the power-to-power (P2P) conversion efficiency is about 30.78 % without taking into account other limited power consumption (calculated by Eq. (S10)). The steam Rankine cycle, as it is currently implemented, significantly restricts further improvements in P2P conversion efficiency. This limitation arises primarily from the inherent thermodynamic constraints of the cycle, which dictate the maximum efficiency achievable based on the temperature and pressure conditions of the steam. Therefore, implementing the steam reheating cycle, the steam regeneration cycle, and the supercritical CO_2 cycles will be effective strategies for further enhancing conversion efficiency. However, the methods and their applications for enhancing the efficiency of P2P conversion are beyond the scope of this study. Based on the given parameters, the main results of the economic evaluations for the business models 1 and 2 are listed in Table 5.

It can be found that running in the semi-continuous operation mode, the operation cost of the business model 1 (732.8 × 10^4 ¥/y) is higher than that of model 2 (81.1 × 10^4 ¥/y). This can primarily be attributed to the higher valley electricity cost in model 1, whereas in model 2, the electricity consumption is derived from photovoltaic and wind power abandoned. Besides, given that the annual utilization hours of model 1 (2920 × 2 h) significantly exceed those of model 2 (880 × 2 h), the operational income of model 1 (1600.1 × 10^4 ¥/y) is correspondingly higher. Therefore, overall, the net yield of model 1 (867.4 × 10^4 ¥/y) is nearly half higher than that of model 2 (471.0 × 10^4 ¥/y). Consequently, model 1 features a *PBP* that is 5 years shorter and an *IRR* that is approximately 10.3 % higher than those of model 2 at the same investment cost. This not only indicates that this engineering application is economically feasible, but also implies that business model 1 utilizing the grid electricity is more favorable and possesses a greater potential for future application and development compared to model 2, on basis of the given project implementation environment.

Table 5
Economic evaluation results.

Business model	Parameter	Value	Unit
1	Y_{op}	1600.1	×10^4 ¥/y
	C_{op}	732.8	×10^4 ¥/y
	Y_{net}	867.4	×10^4 ¥/y
	C_t	4012.0	×10^4 ¥
	PBP	5	Year
	IRR	21.56	%
2	Y_{op}	552.1	×10^4 ¥/y
	C_{op}	81.1	×10^4 ¥/y
	Y_{net}	471.0	×10^4 ¥/y
	C_t	4012.0	×10^4 ¥
	PBP	10	Year
	IRR	11.26	%

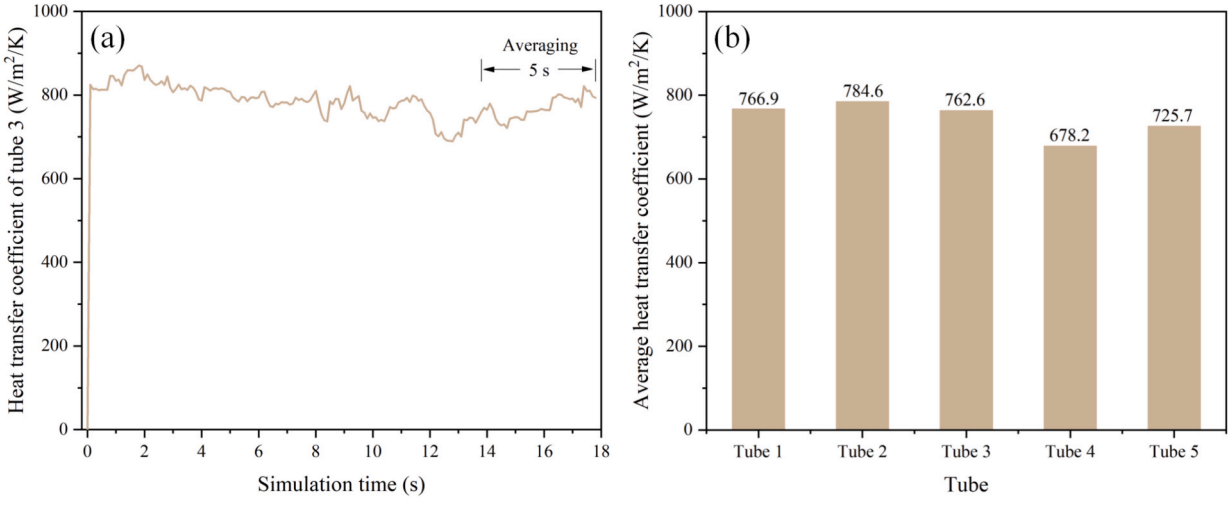

Fig. 7. The diagrams of a) the relationship of the heat transfer coefficient of tube 3 with simulation time and b) the average heat transfer coefficients of tubes 1 to 5.

4.4.2. Sensitivity analysis

Herein, the sensitivities of *IRR*s to several critical factors inherent to business models 1 and 2 are examined, including total investment cost (*F11* or *F21*), peak electricity price (*F12* or *F22*), valley electricity price (*F13*), annual heat storage/release hours (*F14* or *F23*, a single factor when assuming that the annual heat storage hours are equal to the annual heat release hours and both exhibit same variation), life cycle (*F15* or *F24*), comprehensive subsidy for the supply of peak electricity (*F16* or *F25*), and additional government subsidy (*F17* or *F26*). The average sensitivity coefficients of these 13 factors studied are illustrated in Fig. 8 while the detailed sensitivity results can be found in Table S5.

For model 1, its *IRR* is highly dependent on the *F11*, *F12*, and *F14*. A slight change of these factors can significantly affect the economic effectiveness of business model 1, with their absolute sensitivity coefficients of approximately 1.0. In addition, *F13* and *F16* can also exert non-negligible influence on model 1′s *IRR* (their absolute sensitivity coefficients are 0.76). It appears that *F15* and *F17* exhibit the lowest effect. As for model 2, *F21* and *F23* show the most significant influence, followed by *F22* and *F25*. Similarly, two parameters in model 2 (*F24* and *F26*), which is the same as *F15* and *F17* in model 1, also exhibit the lowest sensitivity. In the context of economic analysis and decision-making, this is typically viewed as a positive indicator, signifying that the project possesses robust resilience against risks and can sustain its benefits at a relatively stable level throughout different life cycle stages and government subsidy policies. Furthermore, the results also uncover several potential risk factors (with higher sensitivity coefficients) within the project operating in two business models, which facilitate its promotion, enhance project risk management, and contribute to further optimization and improvement.

Moreover, in order to compare the overall sensitivity of these two operation models to internal parameters, the averages of the absolute values of these sensitivity coefficients are further calculated, which are 0.67 (or 0.65 without *F13*) for model 1 and 0.63 for model 2. The finding suggests that, overall, the income stability of model 1 is nearly comparable to that of model 2, with model 1 showing a marginally higher sensitivity to its internal parameters than model 2. In other words, model 2 is somewhat less dependent on environmental parameters, thereby its ability to resist risks can be considered to be slightly stronger than that of model 1.

Overall, the economic analysis of the EIHS-MBHR engineering application suggests that the business model 1 is more cost-effective but demonstrates a marginally lower risk resistance compared to model 2. It should also be noted that business model 2 is location-dependent and typically more suitable for implementation in areas with a significant amount of abandoned photovoltaic and wind power, such as northwest of China. In contrast, business model 1 has no strong location dependence, but is highly dependent on the peak-valley price difference, thereby it is more appropriate for cities where power supply and demand do not match, such as Shanghai, China. Therefore, in addition to considering the cost-effectiveness and risk resistance capacity, it is recommended to select the business model based on the region's endowment of photovoltaic and wind energy, as well as the current state of power supply and demand.

5. Conclusions

In this work, an innovative electro-thermal energy storage (ETES) system combining electromagnetic induction (EI) heat storage with moving bed heat release (EIHS-MBHR) is proposed and further detailed with system descriptions, design criteria, and an exploration into its engineering applications. To further investigate the EIHS-MBHR system's technical viability, a numerical simulation method grounded in CFD-DEM has been established, initially validated, and subsequently utilized for exploratory simulations in an EI heater unit and a tubular MBHE unit. Additionally, a comprehensive economic evaluation, including a detailed sensitivity analysis, has been conducted to further assess its economic feasibility. The main conclusions are listed as below:

(1) The uniform radial temperature distribution and adjustable temperature rise rate highlight the advantages of the EI heater unit, while the used conductive stainless steel particles also exhibit a satisfactory heat storage density.
(2) The heat transfer intensity in the tubular moving bed heat exchanger (MBHE) unit ranges from 678.2 W/m^2/K to 784.6 W/

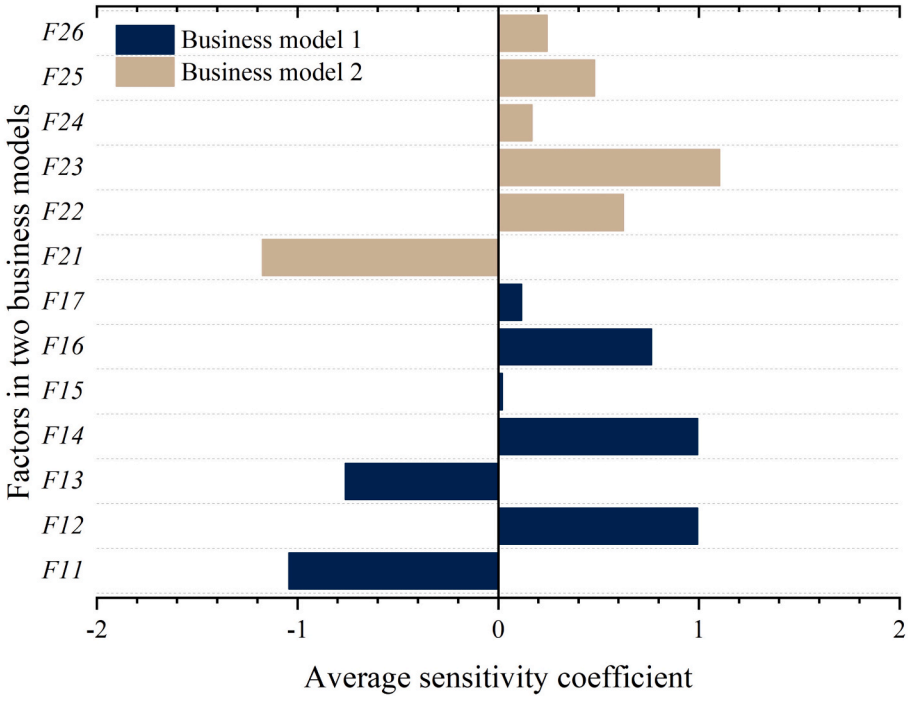

Fig. 8. Average sensitivity coefficients of different factors in two business models. A negative value (indicated by a symbol "-" and a lighter color) signifies a negative relationship, whereas positive values denote a positive relationship.

m^2/K. Due to the high thermal conductivity of the metal particles, the heat exchanger shows satisfactory heat release performance. This advantage precisely addresses the need for timely peak power supply and reduces heat exchanger investment.

(3) By using EI heater and moving bed heat exchanger, the power-to-power (P2P) conversion efficiency of the EIHS-MBHR system is approximately 30.78 %, excluding other minor power consumption.

(4) The proposed ETES system possesses three different operational modes, which are batch operation mode, semi-continuous operation mode (employed by this engineering application), and continuous operation mode, as well as at least two business models for supplying peak electricity, named as model 1 (using valley power) and model 2 (using abandoned photovoltaic and wind power).

(5) The results of preliminary economic evaluation show that the payback periods (*PBP*s) of business models 1 and 2 are 5 years and 10 years, respectively, with corresponding internal rates of return of 21.56 % and 11.26 %. This reveals the acceptable economic feasibility of the proposed engineering application. Besides, it is also found that the business model 1 is more cost-effective but demonstrates a marginally lower risk resistance compared to model 2.

In summary, this study aims to offer valuable insights into the advanced enhancement and development of the ETES system, as well as its future engineering applications. In the future, there is a need to solve the following problems: 1) the detailed, complete and accurate EI heating model for a multi-particle system remains to be studied and established; 2) in order to further clarify the technical feasibility, it is necessary to conduct whole process simulations and corresponding experiments; and 3) further specific economic analysis for specific cities or regions with distinct characteristics is also required.

CRediT authorship contribution statement

Weiqin Lu: Writing – original draft, Validation, Software, Methodology, Investigation, Formal analysis, Data curation. **Xueyu Tang:** Writing – original draft, Software, Investigation, Formal analysis. **Yang Zhang:** Writing – review & editing, Supervision, Conceptualization. **Weiliang Wang:** Writing – review & editing, Supervision. **Tuo Zhou:** Writing – review & editing, Supervision, Software. **Hai Zhang:** Writing – review & editing, Supervision, Conceptualization. **Junfu Lyu:** Writing – review & editing, Validation, Supervision, Conceptualization. **Xiwei Ke:** Writing – review & editing, Supervision, Data curation, Conceptualization.

Declaration of competing interest

The authors declare that they have no known competing financial interests or personal relationships that could have appeared to influence the work reported in this paper.

Acknowledgments

This research was supported by the National Key Research and Development Program Project (2022YFE0117700) and the Program of Beijing Huairou Laboratory (ZD2023008A).

Appendix A. Supplementary data

Supplementary data to this article can be found online at https://doi.org/10.1016/j.enconman.2025.119974.

Data availability

Data will be made available on request.

References

[1] IEA. Renewables 2024.
[2] Liu X, Wu Y, Li H, Zhou H. Design and development of pilot plant applied to wind and light abandonment power conversion: electromagnetic heating of solid particles and steam generator. J Clean Prod 2024;470:143313. https://doi.org/10.1016/j.jclepro.2024.143313.
[3] Stack DC, Curtis D, Forsberg C. Performance of firebrick resistance-heated energy storage for industrial heat applications and round-trip electricity storage. Appl Energy 2019;242:782–96. https://doi.org/10.1016/j.apenergy.2019.03.100.
[4] Hassan Q, Hsu CY, Mounich K, Algburi S, Jaszczur M, Telba AA, et al. Enhancing smart grid integrated renewable distributed generation capacities: Implications for sustainable energy transformation. Sustain Energy Technol Assessments 2024;66:103793. https://doi.org/10.1016/j.seta.2024.103793.
[5] Zhao Y, Song J, Liu M, Zhao Y, Olympios AV, Sapin P, et al. Thermo-economic assessments of pumped-thermal electricity storage systems employing sensible heat storage materials. Renew Energy 2022;186:431–56. https://doi.org/10.1016/j.renene.2022.01.017.
[6] Baak JA, Pozarlik AK, Arentsen MJ, Brem G. Techno-economic study of a zero-emission methanol based energy storage system. Energy Convers Manag 2019;182:530–45. https://doi.org/10.1016/j.enconman.2018.12.015.
[7] Bio Gassi K, Guene Lougou B, Baysal M, Ahouannou C. Thermal and electrical performance analysis of induction heating based-thermochemical reactor for heat storage integration into power systems. Int J Energy Res 2021;45:17982–8001. https://doi.org/10.1002/er.6947.
[8] Mousavi GSM, Faraji F, Majazi A, Al-Haddad K. A comprehensive review of Flywheel Energy Storage System technology. Renew Sustain Energy Rev 2017;67:477–90. https://doi.org/10.1016/j.rser.2016.09.060.
[9] Kong Y, Kong Z, Liu Z, Wei C, Zhang J, An G. Pumped storage power stations in China: the past, the present, and the future. Renew Sustain Energy Rev 2017;71:720–31. https://doi.org/10.1016/j.rser.2016.12.100.
[10] Jia J, Seitz LC, Benck JD, Huo Y, Chen Y, Ng JWD, et al. Solar water splitting by photovoltaic-electrolysis with a solar-to-hydrogen efficiency over 30%. Nat Commun 2016;7:1–6. https://doi.org/10.1038/ncomms13237.
[11] Fereidooni M, Mostafaeipour A, Kalantar V, Goudarzi H. A comprehensive evaluation of hydrogen production from photovoltaic power station. Renew Sustain Energy Rev 2018;82:415–23. https://doi.org/10.1016/j.rser.2017.09.060.
[12] Yong Q, Tian Y, Qian X, Li X. Retrofitting coal-fired power plants for grid energy storage by coupling with thermal energy storage. Appl Therm Eng 2022;215:119048. https://doi.org/10.1016/j.applthermaleng.2022.119048.
[13] Desrues T, Ruer J, Marty P, Fourmigué JF. A thermal energy storage process for large scale electric applications. Appl Therm Eng 2010;30:425–32. https://doi.org/10.1016/j.applthermaleng.2009.10.002.
[14] Ma Z, Wang X, Davenport P, Gifford J, Cook K, Martinek J, et al. System and component development for long-duration energy storage using particle thermal energy storage. Appl Therm Eng 2022;216:119078. https://doi.org/10.1016/j.applthermaleng.2022.119078.
[15] Cisek P, Taler D. Numerical analysis and performance assessment of the Thermal Energy Storage unit aimed to be utilized in Smart Electric Thermal Storage (SETS). Energy 2019;173:755–71. https://doi.org/10.1016/j.energy.2019.02.096.
[16] Maruf MNI, Morales-España G, Sijm J, Helistö N, Kiviluoma J. Classification, potential role, and modeling of power-to-heat and thermal energy storage in energy systems: a review. Sustain Energy Technol Assessments 2022;53. https://doi.org/10.1016/j.seta.2022.102553.
[17] Yu Y, Nie F, Bai F, Liu H, Wang Z. Development and testing of a 200 kW tube bundle moving packed bed electrical heating device and test facility. Int Commun Heat Mass Transf 2023;143:106686. https://doi.org/10.1016/j.icheatmasstransfer.2023.106686.
[18] Bio Gassi K, Guene Lougou B, Baysal M. Performance analysis of induction heated-porous thermochemical energy storage for heat applications in power systems. Appl Therm Eng 2022;217:119226. https://doi.org/10.1016/j.applthermaleng.2022.119226.
[19] Frogner K, Andersson M, Cedell T, Svensson L, Jeppsson P, Ståhl J-E. Industrial heating using energy efficient induction technology. Proc Proc 44th CIRP Int Conf Manuf Syst. 2011.
[20] Lucia O, Maussion P, Dede EJ, Burdio JM. Induction heating technology and its applications: Past developments, current technology, and future challenges. IEEE Trans Ind Electron 2014;61:2509–20. https://doi.org/10.1109/TIE.2013.2281162.
[21] Kulkarni NJ, Mandal D, Mathpati CS, Dalvi VH. Modeling and validation of heat transfer in packed bed with internal heat generation. Heat Transf 2020;49:2961–76. https://doi.org/10.1002/htj.21755.
[22] Hassan OH, Sultan GI, Sabry MN, Hegazi AA. Investigation of heat transfer and pressure drop in a porous media with internal heat generation. Case Stud Therm Eng 2022;32:101849. https://doi.org/10.1016/j.csite.2022.101849.
[23] Meng X, Sun Z, Xu G. Single-phase convection heat transfer characteristics of pebble-bed channels with internal heat generation. Nucl Eng Des 2012;252:121–7. https://doi.org/10.1016/j.nucengdes.2012.05.041.
[24] Catton I, Jakobsson JO. The effect of pressure on dryout of a saturated bed of heat-generating particles. J Heat Transfer 1987;109:185–95. https://doi.org/10.1115/1.3248042.

[25] Schäfer P, Lohnert G. Boiling experiments for the validation of dryout models used in reactor safety. Nucl Eng Des 2006;236:1511–9. https://doi.org/10.1016/j.nucengdes.2006.03.046.
[26] Schäfer P, Groll M, Kulenovic R. Basic investigations on debris cooling. Nucl Eng Des 2006;236:2104–16. https://doi.org/10.1016/j.nucengdes.2006.03.033.
[27] Deng Z. Experimental study of single-phase forced convection heat transfer in pebble-bed channels with internal heat source. Master Thesis; 2011.
[28] Diago M, Iniesta AC, Soum-Glaude A, Calvet N. Characterization of desert sand to be used as a high-temperature thermal energy storage medium in particle solar receiver technology. Appl Energy 2018;216:402–13. https://doi.org/10.1016/j.apenergy.2018.02.106.
[29] Allen KG, Von Backström TW, Kröger DG. Packed rock bed thermal storage in power plants: design considerations. Energy Proc 2014;49:666–75. https://doi.org/10.1016/j.egypro.2014.03.072.
[30] Tetteh S, Yazdani MR, Santasalo-Aarnio A. Cost-effective Electro-Thermal Energy Storage to balance small scale renewable energy systems. J Energy Storage 2021;41:102829. https://doi.org/10.1016/j.est.2021.102829.
[31] Wu C, Yang H, He X, Hu C, Yang L, Li H. Principle, development, application design and prospect of fluidized bed heat exchange technology: comprehensive review. Renew Sustain Energy Rev 2022;157:112023. https://doi.org/10.1016/j.rser.2021.112023.
[32] Ma Z, Gifford J, Wang X, Martinek J. Electric-thermal energy storage using solid particles as storage media. Joule 2023;7:843–8. https://doi.org/10.1016/j.joule.2023.03.016.
[33] Ma Z, Wang X, Davenport P, Gifford J, Martinek J. Preliminary component design and cost estimation of a novel electric-thermal energy storage system using solid particles. J Sol Energy Eng Trans ASME 2022;144. https://doi.org/10.1115/1.4053256.
[34] Ma Z, Glatzmaier G, Mehos M. Fluidized bed technology for concentrating solar power with thermal energy storage. J Sol Energy Eng Trans ASME 2014;136. https://doi.org/10.1115/1.4027262.
[35] Lu W, Ma C, Liu D, Zhao Y, Ke X, Zhou T. A comprehensive heat transfer prediction model for tubular moving bed heat exchangers using CFD-DEM: validation and sensitivity analysis. Appl Therm Eng 2024;247:123072. https://doi.org/10.1016/j.applthermaleng.2024.123072.
[36] Cheng Z, Tan Z, Guo Z, Yang J, Wang Q. Technologies and fundamentals of waste heat recovery from high-temperature solid granular materials. Appl Therm Eng 2020;179:115703. https://doi.org/10.1016/j.applthermaleng.2020.115703.
[37] Laubscher HF, Albrecht KJ, Ho CK. High-temperature particle flow testing in parallel plates for particle-to-supercritical CO2 heat exchanger applications. n.d.
[38] Feng J, Dong H, Gao J-Y, Liu J-Y, Liang K. Theoretical and experimental investigation on vertical tank technology for sinter waste heat recovery. J Cent South Univ 2017;24:2281–7. https://doi.org/10.1007/s11771-017-3639-x.
[39] Bauer T, Odenthal C, Bonk A. Molten salt storage for power generation. Chem-Ing-Tech 2021;93:534–46. https://doi.org/10.1002/cite.202000137.
[40] Atkhen K, Berthoud G. SILFIDE experiment: coolability in a volumetrically heated debris bed. Nucl Eng Des 2006;236:2126–34. https://doi.org/10.1016/j.nucengdes.2006.03.061.
[41] Tanabe K. Selective electromagnetic induction heating of metal particles in molten salt for tritium extraction: a systematic numerical investigation. Fusion Eng Des 2021;163:112177. https://doi.org/10.1016/j.fusengdes.2020.112177.
[42] Shinohara N, Arimasa S, Kashimura K, Mitani T. Study on microwave absorption property of multi metal particles by electromagnetic simulation. In: Asia-Pacific Microw Conf Proceedings; 2018. p. 588–90. https://doi.org/10.23919/APMC.2018.8617367.
[43] Suzuki M, Ignatenko M, Yamashiro M, Tanaka M, Sato M. Numerical study of microwave heating of micrometer size metal particles. ISIJ Int 2008;48:681–4. https://doi.org/10.2355/isijinternational.48.681.
[44] Duquenne P, Deltour A, Lacoste G. Application of inductive heating to granular media: modelling of electrical phenomena. Can J Chem Eng 1994;72:975–81. https://doi.org/10.1002/cjce.5450720606.
[45] Ignatenko M, Tanaka M, Sato M. Absorption of microwave energy by a spherical nonmagnetic metal particle. Jpn J Appl Phys 2009;48. https://doi.org/10.1143/JJAP.48.067001.
[46] Lu J, Zhang H. A deep study on a particle-water coupled fast induction heating system. ASME J Heat Mass Transf 2023;145. https://doi.org/10.1115/1.4062307.
[47] Wang Z, Liu M. Semi-resolved CFD–DEM for thermal particulate flows with applications to fluidized beds. Int J Heat Mass Transf 2020;159:120150. https://doi.org/10.1016/j.ijheatmasstransfer.2020.120150.
[48] Marchelli F, Moliner C, Bosio B, Arato E. A CFD-DEM sensitivity analysis: the case of a pseudo-2D spouted bed. Powder Technol 2019;353:409–25. https://doi.org/10.1016/j.powtec.2019.05.035.
[49] Lu W, Li Z, Tang X, Liu D, Ke X, Zhou T. Simulation study on heat and mass transfer characteristics within tubular moving bed heat exchangers. Case Stud Therm Eng 2024;61:105008. https://doi.org/10.1016/j.csite.2024.105008.
[50] Li L, Liu Z, Xu J, Ma X. Discrete element simulation study on particle segregation effect of a hemispherical shell swing-oscillating trough under combination swing-oscillating. Trans Electr Electron Mater 2020;21:249–57. https://doi.org/10.1007/s42341-020-00173-4.
[51] Tian X, Guo Z, Jia H, Yang J, Wang Q. Numerical investigation of a new type tube for shell-and-tube moving packed bed heat exchanger. Powder Technol 2021;394:584–96. https://doi.org/10.1016/j.powtec.2021.08.080.
[52] Hertel JD, Zunft S. Experimental validation of a continuum model for local heat transfer in shell-and-tube moving-bed heat exchangers. Appl Therm Eng 2022;206. https://doi.org/10.1016/j.applthermaleng.2022.118092.
[53] Tian X, Jia H, Zhang J, Guo Z, Yang J, Wang Q. Heat transfer characteristic of particle flow around the out-wall of different geometries. Energy 2023;280. https://doi.org/10.1016/j.energy.2023.128217.